Shock Waves (2004) 13: 327–337
Digital Object Identifier (DOI) 10.1007/s00193-003-0223-0

Shock Waves

*Original article*

# Unsteady convective surface heat flux measurements on cylinder for CFD code validation

T. Saito[1], V. Menezes[1], T. Kuribayashi[1], M. Sun[1], G. Jagadeesh[2], K. Takayama[1]

[1] Institute of Fluid Science, Tohoku University, 2-1-1 Katahira, Aoba-ku, Sendai 980-8577, Japan

[2] Department of Aerospace Engineering, Indian Institute of Science, Bangalore-560 012, India

Received 27 August 2003 / Accepted 11 November 2003
Published online 17 February 2004 – © Springer-Verlag 2004
Communicated by H. Grönig

**Abstract.** The surface convective heat transfer rates to a cylinder have been measured using platinum thin film gauges in a shock tube and the results have been used to validate two numerical codes. The investigations have been carried out at different incident shock Mach numbers and flow Reynolds numbers. The measured and simulated results give an insight into the transient flow fields around the model in the shock tube and are a valuable means of complementing the numerical and experimental techniques used in this study.

**Key words:** Platinum thin film gauge, Heat flux, Shock tube, Code validation

**Nomenclature**

Symbols

| | |
|---|---|
| $c_p$ | specific heat at constant pressure, $J{\cdot}kg^{-1}{\cdot}K^{-1}$ |
| $E_f$ | thin film initial voltage, V |
| E(t) | thin film voltage at time t, V |
| $H_0$ | flow stagnation enthalpy, $J{\cdot}kg^{-1}$ |
| $H_w$ | enthalpy at wall, $J{\cdot}kg^{-1}$ |
| I | constant current through the gauge, mA |
| k | thermal conductivity, $W{\cdot}m^{-1}{\cdot}K^{-1}$ |
| L | thickness of thin film gauge, μm |
| $M_S$ | incident shock Mach number |
| $M_2$ | flow Mach number behind incident shock wave |
| $p_1$ | test gas fill pressure, kPa |
| $p_2$ | pressure behind incident shock wave, kPa |
| $p_4$ | driver gas pressure, kPa |
| $\dot{q}(t)$ | heat flux at time t, $W/cm^2$ |
| $Re_\infty$ | free stream unit Reynolds number, $m^{-1}$ |
| $Re_d$ | Reynolds number based on body diameter |
| r | thin film initial resistance, Ω |
| St | Stanton number |
| Sr | Strouhal number |
| T | temperature, K |
| $T_0$ | flow total temperature, K |
| $T_1$ | test gas initial temperature, K |
| $T_2$ | temperature behind incident shock wave, K |
| $T_w$ | test model wall initial temperature, K |
| t | time, s |
| $\Delta$ T | change in gauge temperature, K |
| $V_\infty$ | free stream velocity, m/s |
| $\Delta$ V | voltage change across the gauge, V |
| y | distance in y direction, m |

Greek letters

| | |
|---|---|
| $\alpha$ | temperature coefficient of resistance of thin film, $K^{-1}$ |
| $\beta$ | $(k\rho c_p)^{1/2}$ for thin film backing material, $J{\cdot}m^{-2}{\cdot}K^{-1}{\cdot}s^{-1/2}$ |
| $\gamma$ | specific heat ratio |
| $\rho$ | density, $kg/m^3$ |
| $\rho_2$ | density behind incident shock wave, $kg/m^3$ |
| $\rho_\infty$ | free stream (flow) density, $kg/m^3$ |
| $\tau$ | time variable, s |
| $\phi$ | gauge location angle on cylinder surface, ° |

## 1 Introduction

With the tremendous advancement in the computational powers and methodologies in the recent years, Computational Fluid Dynamics (CFD) has emerged as a very promising area of research with an extensive use of CFD codes in several engineering applications including aerodynamics. However, these codes need to be validated against accurate and reliable data generated out of well-designed experimental techniques before their application to real time tasks. Hence, in the development of a CFD code, especially for aerodynamic applications, the ground testing

*Correspondence to* T. Saito
(e-mail: saito@bellanca.ifs.tohoku.ac.jp)

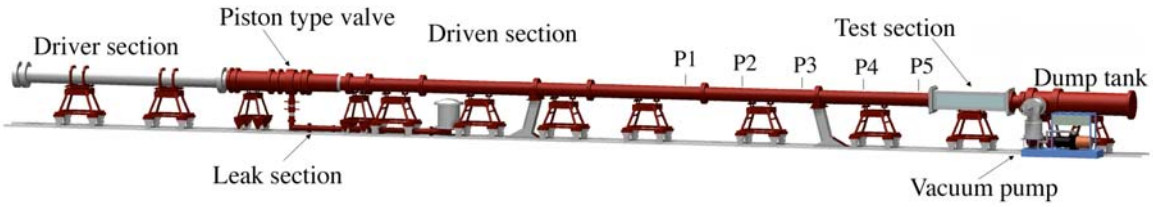


**Fig. 1.** Schematic of diaphragm-less shock tube; P1–P5: pressure transducer locations

facilities play an important role in providing vital design data as well as an insight into unresolved aspects of flow physics.

Flows in shock tubes are characterized by their unsteadiness due to a limited in available test time . It has been reported that numerical solutions of the unsteady Euler equations precisely reproduce shock propagation, reflections from walls, and interaction with bodies. In other words, the current CFD codes are able to simulate unsteady convection-dominated flows. However, the deviation of CFD results from experiments may become noticeable in viscosity-dominated flows, such as shock/boundary layer interaction and flows in wakes. Therefore, perfect agreement of the viscosity-dominated parameters such as surface heat conduction, skin friction etc. is seldom achieved or observed in literature.

With the intention of validating an in-house CFD code (Sun and Takayama, 1999) and a commercial code on the results of surface convective heating rates to a body in a high speed flow, an accurate experimental technique for measuring heat transfer using platinum thin film sensors was developed during the course of this current study. The heat transfer rates to the surface of a concentric cylinder have been measured in a diaphragm-less shock tube at different incident shock Mach numbers and flow Reynolds numbers. The diaphragm-less shock tube used in the current study has an extremely good repeatability and hence is capable of generating very reliable data for such validation purposes.

In this paper, we present the details of the experimental set-up, the surface heat flux measurement technique, and some of the experimental and CFD results on the surface convective heat transfer rates as well as the unsteady flow fields around a circular cylinder.

## 2 Experimental setup

### 2.1 Shock tube facility

The surface convective heat transfer rates to a cylinder in a supersonic flow are measured in a diaphragm-less steel shock tube with a rectangular cross section of 100 mm×180 mm. Figure 1 gives the schematic of the shock tube used in the present study. It has a 6 m long driver section and an 18 m long driven section that are separated by a piston type valve. The piston arrangement and its operation are shown in Fig. 2. The head of the piston blocks the driver section, completely isolating it from the driven section while the rear end of the piston is exposed to a leak section through a hollow tube. The annular space between the piston arrangement and the shock tube inner wall provides a passage for the driver gas to flow into the driven section during the operation. The tube connecting the piston rear end and the leak section is divided into three segments separated by two Mylar diaphragms. The diaphragm stations are indicated in Fig. 2a.

Although the basic operation of the piston valve is described by Meguro et al. (1997), it is repeated here for completeness. Evacuating the leak section would retract the piston thereby connecting the driver and driven sections of the shock tube, enabling absolute evacuation of the entire tube. After evacuating the entire shock tube, the leak section is brought back to atmospheric pressure, making the piston retrace to its original position due to the pressure difference between the shock tube and the leak section, which would close the driver section isolating it from the driven section. The leak section is evacuated again after placing the circular Mylar diaphragms in their stations. The driver section is then filled with the driver gas to a desired pressure and the auxiliary high-pressure chamber behind the piston is pressurized to a level greater than that of the driver section to keep the driver section closed with the piston. The middle pressure chamber, which exists between the leak section and the auxiliary high-pressure chamber, is also pressurized to a moderate level in order to keep the Mylar diaphragms intact by reducing the pressure differences on them. The driven section of the shock tube is then filled with the test gas to a desired pressure. The system is totally leak proof enabling the operator to precisely maintain the pressures in the driver and driven sections to the desired values.

During operation of the shock tube, the middle pressure chamber is further pressurized until the Mylar diaphragm at the second station (Diaphragm 2) ruptures, which would increase the pressure difference on the Mylar diaphragm at the first station (Diaphragm 1), which in turn would also yield. This exposes the rear end of the piston to a vacuum in the leak section and the piston retracts, opening the driver section. The driver gas accelerates into the driven section through the annular space between the piston arrangement and the shock tube inner wall giving rise to a shock wave a little downstream, which propagates through the driven section imparting pressure and kinetic energy to the test gas. The piston actuation process is schematically described through Figs. 2b–d. The piston is equipped with a quick retracting mechanism which enables sudden acceleration of the piston from its initial po-

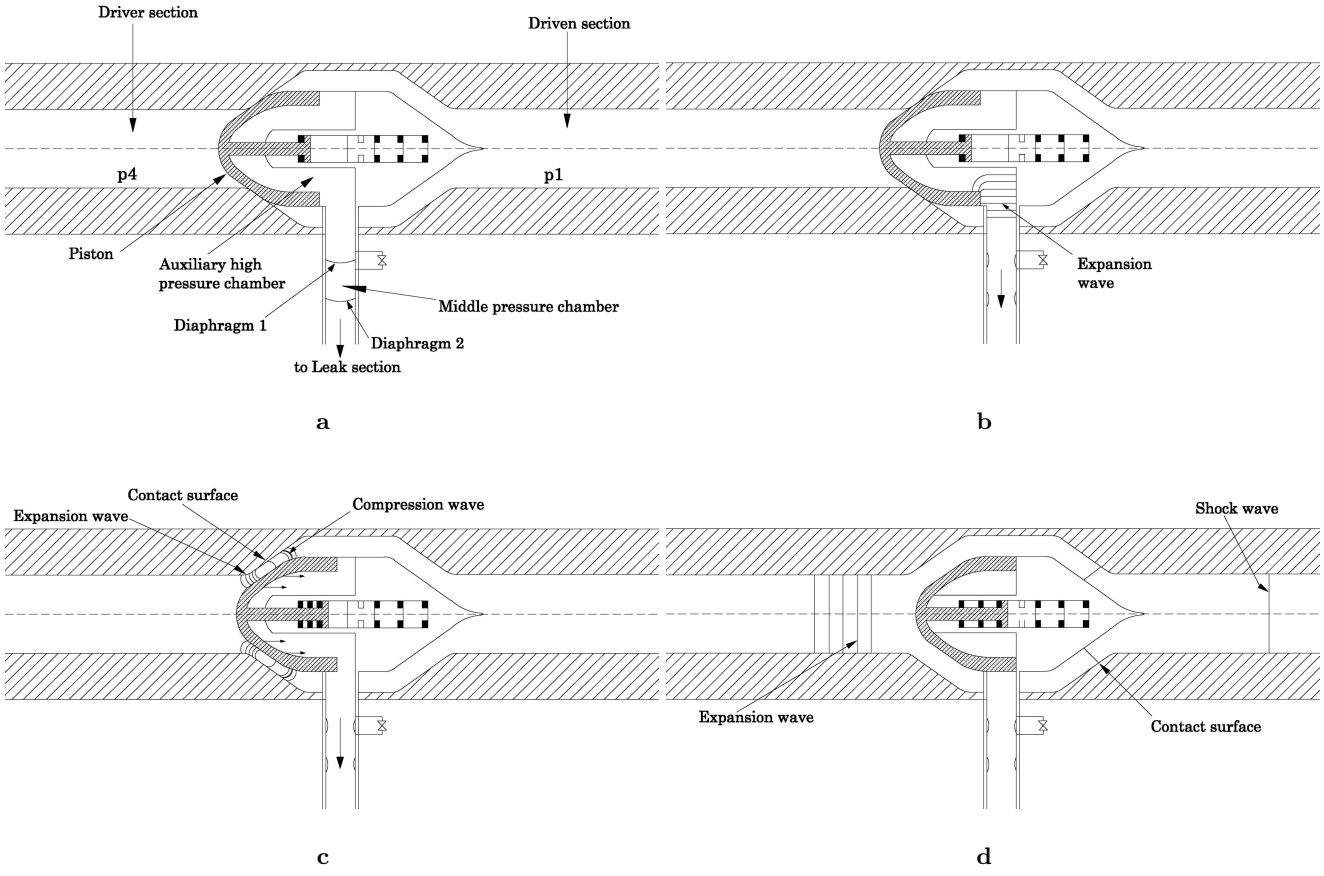


**Fig. 2a–d.** Arrangement of piston type valve and its operation during shock tube experiments

sition, and also a smooth decelerating mechanism which prevents the piston from getting damaged when it comes to rest in its retracted position. The shape of the front portion of the piston prevents sudden expansion of the driver gas thereby increasing the available test time. The shock tube has a circular-to-rectangular cross section transition region that is about 1.2 m long between the piston valve and the driven section, which gradually transforms the circular driver/valve section into a rectangular driven section, enabling smooth transition of the flow with a minimum of three-dimensional transitional wave interactions and flow perturbations. However, these perturbations do not influence the process of measurement in the test section since the transition zone is far upstream.

The driven section of the shock tube is equipped with a series of pressure ports for monitoring the static pressures behind the moving primary shock wave and also to measure the shock speed. Figure 3 gives an $x$-$t$ diagram for a typical shot ($M_S = 2.43$) indicating the available test time in the test section of the shock tube. The test time is terminated by the arrival of the reflected expansion wave head from the driver end as indicated in Fig. 3 for moderate incident shock Mach numbers, and the arrival of the contact surface terminates the test time for the shots with stronger incident shock waves. The pressure history

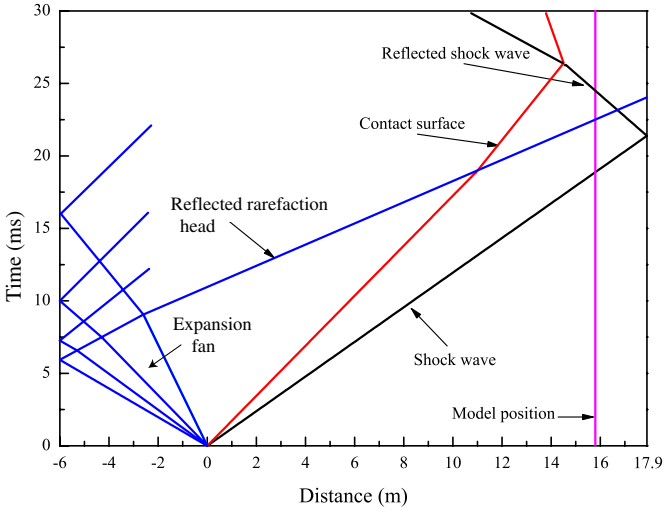


**Fig. 3.** A typical $x$-$t$ diagram ($M_S = 2.43$)

recorded by the transducer very close to the test section is also useful to some extent in determining the steady flow duration in the test section.

The 1.5 m long rectangular test section, located at the end of the driven section of the shock tube is equipped

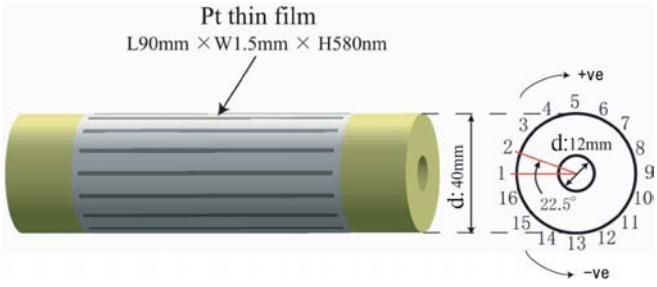


**Fig. 4.** Test model with Platinum (Pt) thin film gauges

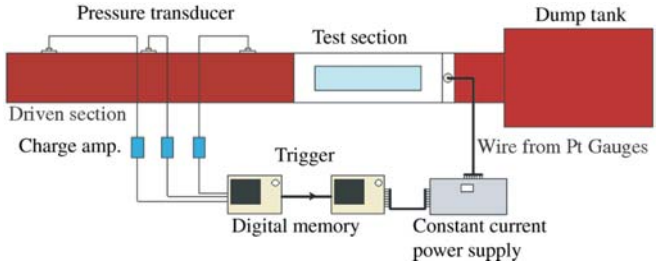


**Fig. 5.** Schematic diagram of the experimental setup for heat transfer measurements

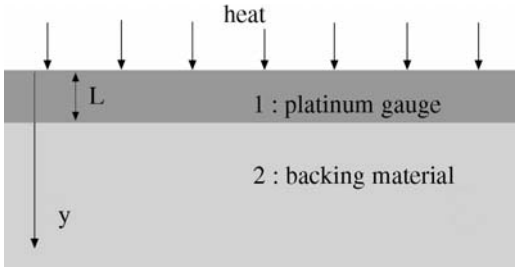


**Fig. 6.** Model for one-dimensional heat transfer theory

with optical windows and ports for electrical lead connections. Surface measurements and visualization experiments can conveniently be carried out on models up to 50 mm in size in this test facility. The piston type valve arrangement enables extremely good repeatability in the experiments with a maximum shot to shot variation of ±0.3% in shock Mach number. The problem of metal particles from the diaphragms damaging the sensors/model surface, as in the case of conventional shock tubes, is totally eliminated in this case, which makes the sensors/model more durable, enabling better repeatability in the measured data. Hence, this facility makes for an invaluable tool for validation experiments, especially for validating the CFD codes.

## 2.2 Test model and experimental methods

The test model used in the present study is a circular cylinder, fabricated out of a machinable ceramic glass (Photoveel, Sumikin Ceramic and Quartz Co., Japan) as shown in Fig. 4. The ceramic glass used for the model is a suitable backing material for the thermal sensors and is also an extremely good thermal insulator.

Two cylindrical brass attachments are used on either side of the model for the purpose of fastening it in the test section. Platinum thin film sensors are deposited on the surface of the ceramic cylinder, by a vacuum deposition technique, in order to measure the surface heat flux. Sixteen gauges at angular intervals of 22.5° are distributed along the circumference of the cylinder parallel to its longitudinal axis. A silver paste is deposited on both sides of the platinum sensors for soldering the electrical connections.

The platinum thin film gauge is a passive sensor and has to be energized. The sensor is powered using a constant current power supply, through which it is connected to a data acquisition system. In the present case, a constant current of 15 mA is used to energize the sensors, which have an initial resistance of around 45 Ω. The resistance of a platinum thin film sensor is very sensitive to temperature and would increase with the temperature during the supersonic flow over it, which would result in a change in the voltage of the circuitry. This change in voltage with respect to time is the temperature time history at the gauge location on the model surface. For a $\Delta T$ change in the gauge temperature, the change in voltage across the gauge $\Delta V$ is given by the following expression:

$$\Delta V = \alpha r \Delta T I \, . \tag{1}$$

The constant current $I$ through the gauges during the experiments has been kept low (15 mA) so that the self-ohmic heating of the gauges is minimized. Figure 5 gives the experimental setup for the current set of experiments.

The thin film gauge measures the change in surface temperature of the body on which it is mounted and does not function directly as a gauge for the measurement of heat transfer to the body. However, the theory for heat conduction in a non-homogeneous body can be used to relate the surface temperature history to the rate of heat transfer to the body.

Since the thin film gauge is mounted on a backing material, the gauge along with the backing material becomes a non-homogeneous body with two regions, 1 (platinum gauge) and 2 (backing material), as shown in Fig. 6, representing the materials with dissimilar thermal and physical properties. Since the thin film gauge thickness (region 1: L) is 0.5 to 0.8 μm, its edge area would be negligible and hence the lateral heat transfer would be negligibly small in comparison with the longitudinal heat transfer. Hence, it is possible to use a one-dimensional heat conduction model for this analysis. The backing material used in this case is an extremely good thermal insulator and considering a test time of thr order of milliseconds in the shock tube, a 14 mm thick ceramic glass can be considered to be infinitely thick or long for these purposes.

Considering the model shown in Fig. 6, with a transient rate of heat transfer into the body, a general expression for the heat transfer rate is given by Hollis (1995) and is as follows:

$$\dot{q}(t) = \frac{\beta}{\sqrt{\pi}} \left[ \frac{T(t)}{\sqrt{t}} + \frac{1}{2} \int_0^t \frac{T(t) - T(\tau)}{(t-\tau)^{3/2}} d\tau \right] \, . \tag{2}$$

The time dependent relative temperature T(t) in the above equation can be expressed in terms of relative voltage E(t), which is directly proportional to T(t), using (1) and the heat transfer rate can be expressed as below (Vidal, 1956):

$$\dot{q}(t) = \frac{\beta}{\sqrt{\pi}\alpha E_f}\left[\frac{E(t)}{\sqrt{t}} + \frac{1}{2}\int_0^t \frac{E(t)-E(\tau)}{(t-\tau)^{3/2}}d\tau\right], \qquad (3)$$

where $E_f = r{\cdot}\mathrm{I}$, which is a finite value, but is set as the zero level or base level for the measured voltage E(t). A numerical procedure to evaluate the quantity within the brackets in (3) has been given by Cook and Felderman (1966). For a given $E(\tau)$, values of this function can be determined at

$$\tau = t_i = i\Delta t; \quad i = 0, 1, 2, ..., n; \quad \text{where, } \Delta t = t/n.$$

Then $E(\tau)$ can be approximated by a piece-wise linear function of the form

$$E(\tau) = E(t_{i-1}) + \frac{E(t_i) - E(t_{i-1})}{\Delta t}(\tau - t_{i-1}), \qquad (4)$$

where $t_{i-1} \le \tau \le t_i, \quad i = 1, 2, 3, ....., n.$

When $E(\tau)$ from (4) is substituted into (3) and integration is performed, the following expression is obtained:

$$\dot{q}(t) = \frac{\beta}{\sqrt{\pi}\alpha E_f}\left[\frac{E(t_n)}{\sqrt{t_n}} + \sum_{i=1}^{n-1}\left\{\frac{E(t_n)-E(t_i)}{(t_n-t_i)^{\frac{1}{2}}} - \frac{E(t_n)-E(t_{i-1})}{(t_n-t_{i-1})^{\frac{1}{2}}} + 2\frac{E(t_i)-E(t_{i-1})}{(t_n-t_i)^{\frac{1}{2}}+(t_n-t_{i-1})^{\frac{1}{2}}}\right\} + \frac{E(t_n)-E(t_{n-1})}{(\Delta t)^{\frac{1}{2}}}\right]. \qquad (5)$$

The above equation has no integration approximations and the accuracy of the result obtained in using this expression is limited only by the degree to which the true function $E(\tau)$ is approximated by the piecewise linear expression given by (4) (Cook and Felderman, 1966). In the present study, (5) is programmed for repetitive calculations on a PC to provide heat flux values at $n$ discrete points in the time interval $(0, t)$.

To use (5) for obtaining heat flux from the temperature time history data of the thin film gauge, we need the values of $E_f$, $\alpha$, and $\beta$. The initial voltage calculated across each gauge, $E_f$, is based on the initial resistance of the gauge and the constant current fed to it; $\beta$, the gauge backing material property, which is equal to $(k\rho c_p)^{1/2}$ can be obtained by knowing the thermal conductivity, mass density, and specific heat (at constant pressure) of the backing material. The value of $\beta$ thus obtained is 1882 $\mathrm{J{\cdot}m^{-2}{\cdot}K^{-1}{\cdot}s^{-1/2}}$; $\alpha$, the temperature coefficient of resistance of the platinum thin film gauge is obtained from a calibration experiment and is equal to 0.00215 $\mathrm{K^{-1}}$ .

## 3 Results and discussion

### 3.1 Experiments

The convective surface heat transfer measurements on the cylinder are carried out at different incident shock Mach numbers ($\mathrm{M}_S$) of 1.77, 2.43, 3.34, and 4.04 in the shock tube. Typical test conditions in the shock tube are detailed in Table 1. The static pressure behind the incident shock wave at the entry to the test section is monitored, together with the output of the thin film sensors on the model. The shock tube wall pressure at the entry to the test section and the temperature time history signal over the cylinder at the front stagnation point ($\phi = 0°$) obtained during one of the shots are presented in Fig. 7. The steady portion of the elevated wall pressure signal represents the steady flow duration in the test section. The sudden temperature rise at point A in the thin film gauge signal is an indication of the impingement of the incident shock wave at the model.

**Table 1.** Experimental conditions in the shock tube for heat flux measurements

| $\mathrm{M}_S$ | 1.77 | 2.43 | 3.34 | 4.04 |
|---|---|---|---|---|
| $\mathrm{M}_2$ | 0.817 | 1.17 | 1.44 | 1.56 |
| $\mathrm{p}_1$ | 10.1 (Air) | 10.1 (Air) | 3.00 (Air) | 1.00 (Air) |
| $\mathrm{p}_2$ | 35.2 | 67.9 | 38.6 | 18.9 |
| $\mathrm{p}_4$ | 400 ($\mathrm{N}_2$) | 400 (He) | 600 (He) | 600 (He) |
| $\mathrm{T}_1$ | 295.1 | 295.2 | 296.0 | 294.8 |
| $\mathrm{T}_2$ | 445 | 611 | 919 | 1212 |
| $\rho_2$ | 0.275 | 0.387 | 0.146 | 0.054 |
| $\mathrm{Re}_d$ | $1.53 \times 10^5$ | $2.92 \times 10^5$ | $1.29 \times 10^5$ | $5.04 \times 10^4$ |

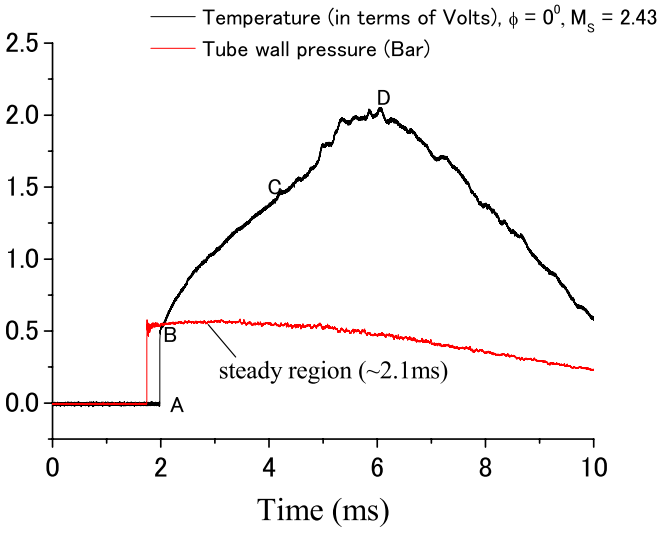


**Fig. 7.** Model stagnation point temperature and tube wall pressure signals indicating flow physics during a typical test

The parabolic rise in the temperature signal between points B and C indicates an establishment of steady supersonic flow over the model and a steady state heat transfer from the gas to the model. The part of the temperature signal between C and D shows fluctuations and deviates from the parabolic shape, which is probably due to some wave interaction. Beyond point D, the temperature signal on the model drops with respect to time which marks the arrival of the rarefaction head from the driver end of the shock tube.

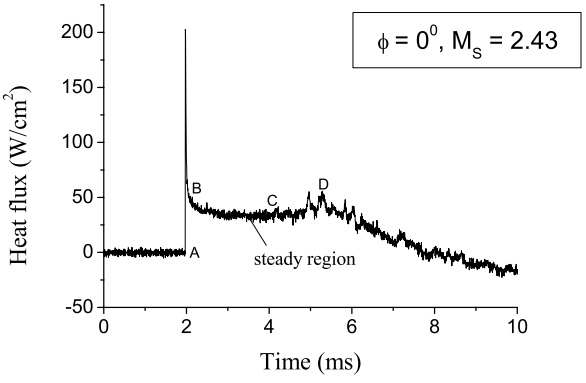


**Fig. 8.** Heat flux signal at the model stagnation point

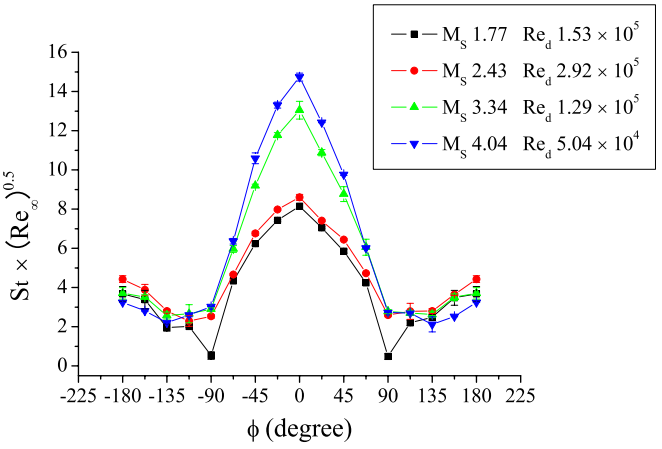


**Fig. 9.** Heat flux distribution along the circumference of the cylindrical model

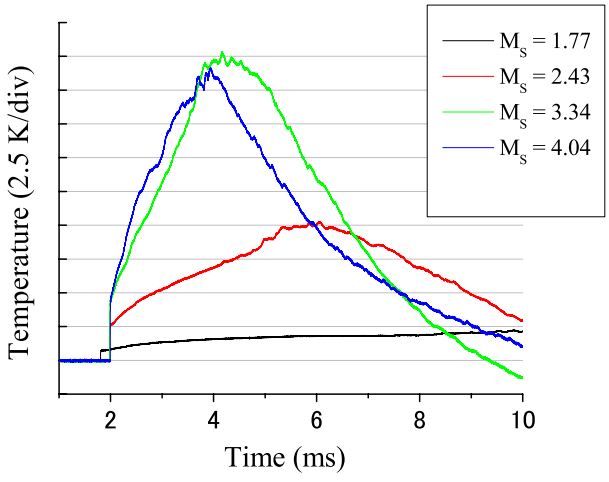


**Fig. 10.** Temperature readings at cylinder stagnation point

Based on (5), the heat flux on the model surface has been numerically evaluated from the temperature-time histories and the heat flux signal corresponding to the temperature signal in Fig. 7 is shown in Fig. 8. The region of steady state heat transfer rate to the body is indicated between points B and C in this figure.

The surface convective heating rates over the cylinder are non-dimensionalized with respect to free stream conditions and are presented in terms of $St \times \sqrt{\mathrm{Re}_\infty}$, where $St$ is the Stanton number, which is defined as:

$$St = \frac{\dot{q}(t)}{\rho_\infty V_\infty (H_0 - H_w)}, \qquad (6)$$

where $H_0 = c_p \times T_0$ and $H_w = c_p \times T_w$.

The gauge locations on the model surface are expressed in terms of angles $\phi$ (degree) measured along the circumference from the front stagnation point of the cylinder. The angular locations of the gauges on the upper and lower sides are marked positive and negative respectively.

The heating rate distributions on the model surface for different incident shock Mach numbers are presented in Fig. 9. Maximum heat transfer occurs at the front stagnation point ($\phi = 0°$) due to a sudden deceleration of the flow behind the normal shock at that point. Relatively low values of heat transfer rates are observed further downstream on the cylinder surface and also in the wake. The trend of heat transfer distribution is comparable from $\phi = 0°$ to $\phi = 90°$ for all the cases and beyond 90° each case has its own pattern. Slight asymmetries have been observed between the values of heat flux on the upper and lower sides of the model because the flow around the cylinder could be very sensitive to small degrees of free stream turbulence and surface roughness (Bearman, 1969; Roshko, 1961).

The temperature readings at the stagnation point and on the upper side of the cylinder are presented in Figs. 10 and 11 respectively, for all the incident shock Mach numbers. The flow separation on the cylinder occurs at an angle greater than 90°, somewhere between 90° and 112.5° for all the cases, which is indicated by the lower and unsteady temperature readings in that region as shown in the figure. The flow separation is known to occur at angles ($\phi$) less than 90° for laminar flows and at angles greater than 90° for turbulent flows (Chang, 1970). The turbulent flow is more capable of resisting the adverse pressure gradient and friction, and the flow separates further downstream compared to the laminar flow. The Reynolds numbers for the experiments in this study have been in the range of $5{\times}10^4$ to $3{\times}10^5$, which fall in both subcritical and critical regimes (Bearman, 1969). Though the Reynolds number $5{\times}10^4$ falls in the subcritical regime, where the flow separation is expected to be of a laminar nature, the separation is still observed at an angle greater than 90°. In this regime of Reynolds numbers the wake is turbulent (Chang, 1970) though the flow separation is of a laminar nature.

The flow around a cylinder and also the heat transfer to a cylinder are generally dominated by periodic vortex shedding (Hermann et al., 1987). In the present study, the vortex shedding phenomenon has been observed in terms of periodically fluctuating temperature signals in the wake of the cylinder at a subcritical Reynolds number of $5 \times 10^4$ ($M_S = 4.04$) as shown in Fig. 11d, ($\phi = 112.5°$). The vortex shedding seems to be regular in the region $\phi = 112.5°$ for this particular Reynolds number as seen from the periodic temperature variations at that location. By taking the separation frequency from the temperature signals the

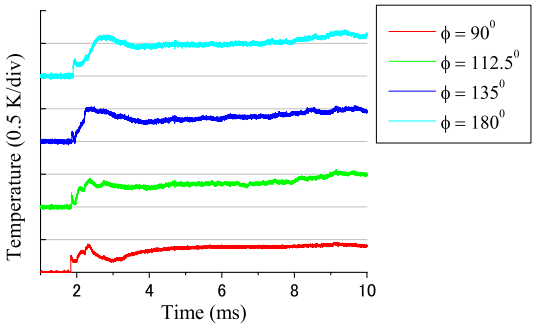


**a** $M_S = 1.77$ ($Re_d = 1.53 \times 10^5$)

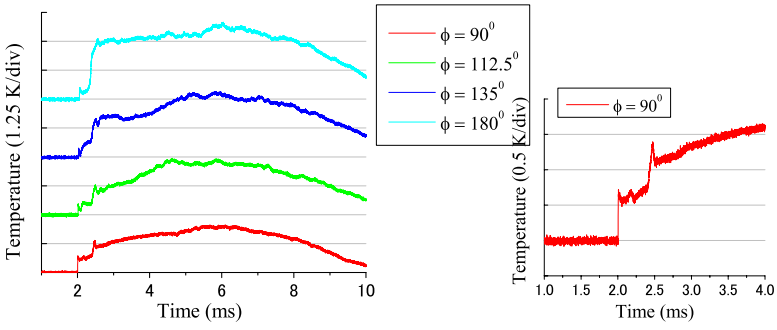


**b** $M_S = 2.43$ ($Re_d = 2.92 \times 10^5$)

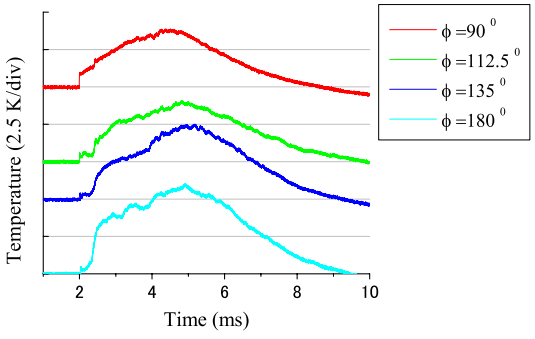


**c** $M_S = 3.34$ ($Re_d = 1.29 \times 10^5$)

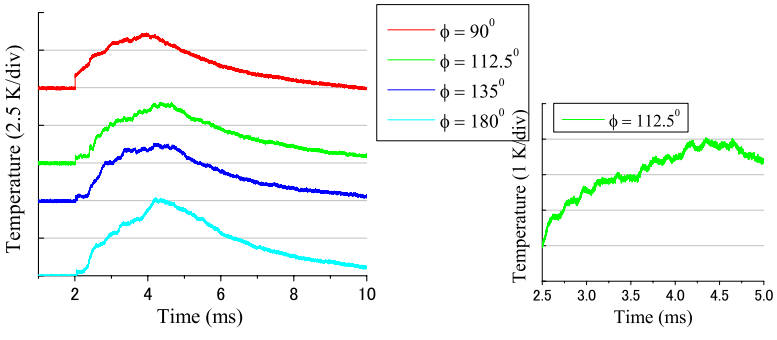


**d** $M_S = 4.04$ ($Re_d = 5.04 \times 10^4$)

**Fig. 11a–d.** Temperature readings on the upper side of the cylinder (Ref. Table 1 for experimental conditions)

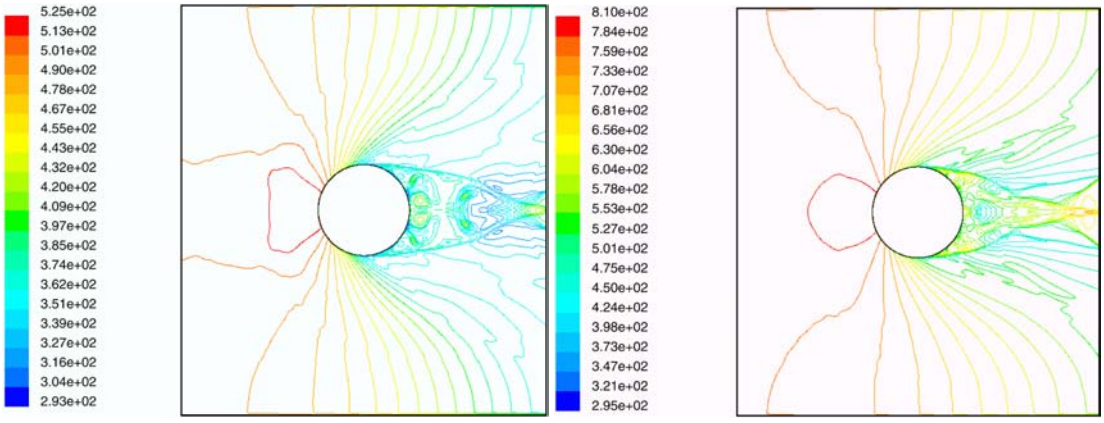


**a** $M_S = 1.77$, $t = 1.07$ ms, $Re_d = 1.53 \times 10^5$ **b** $M_S = 2.43$, $t = 0.986$ ms, $Re_d = 2.92 \times 10^5$

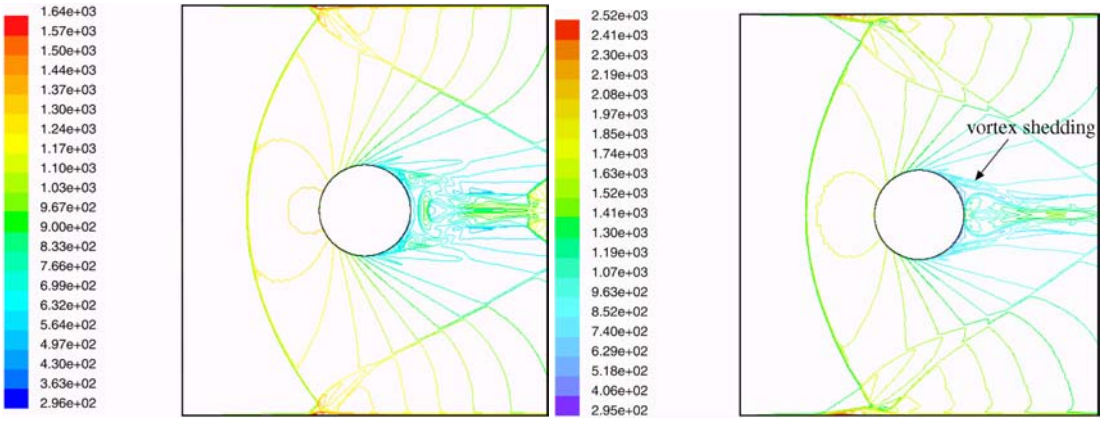


**c** $M_S = 3.34$, $t = 235\,\mu$s, $Re_d = 1.29 \times 10^5$ **d** $M_S = 4.04$, $t = 235\,\mu$s, $Re_d = 5.04 \times 10^4$

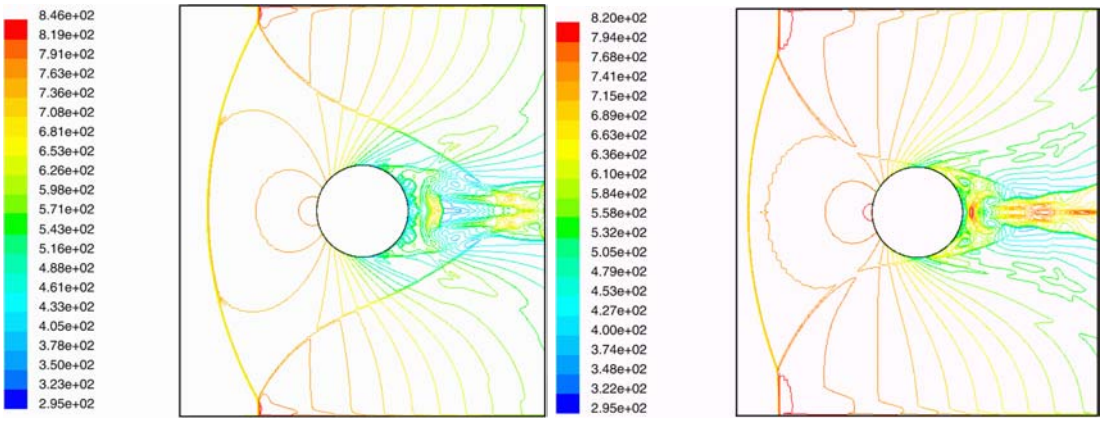


**e** $M_S = 2.43$, $t = 350\,\mu$s **f** $M_S = 2.43$, $t = 450\,\mu$s

**Fig. 12a–f.** Simulated temperature fields (Fluent) around the cylinder

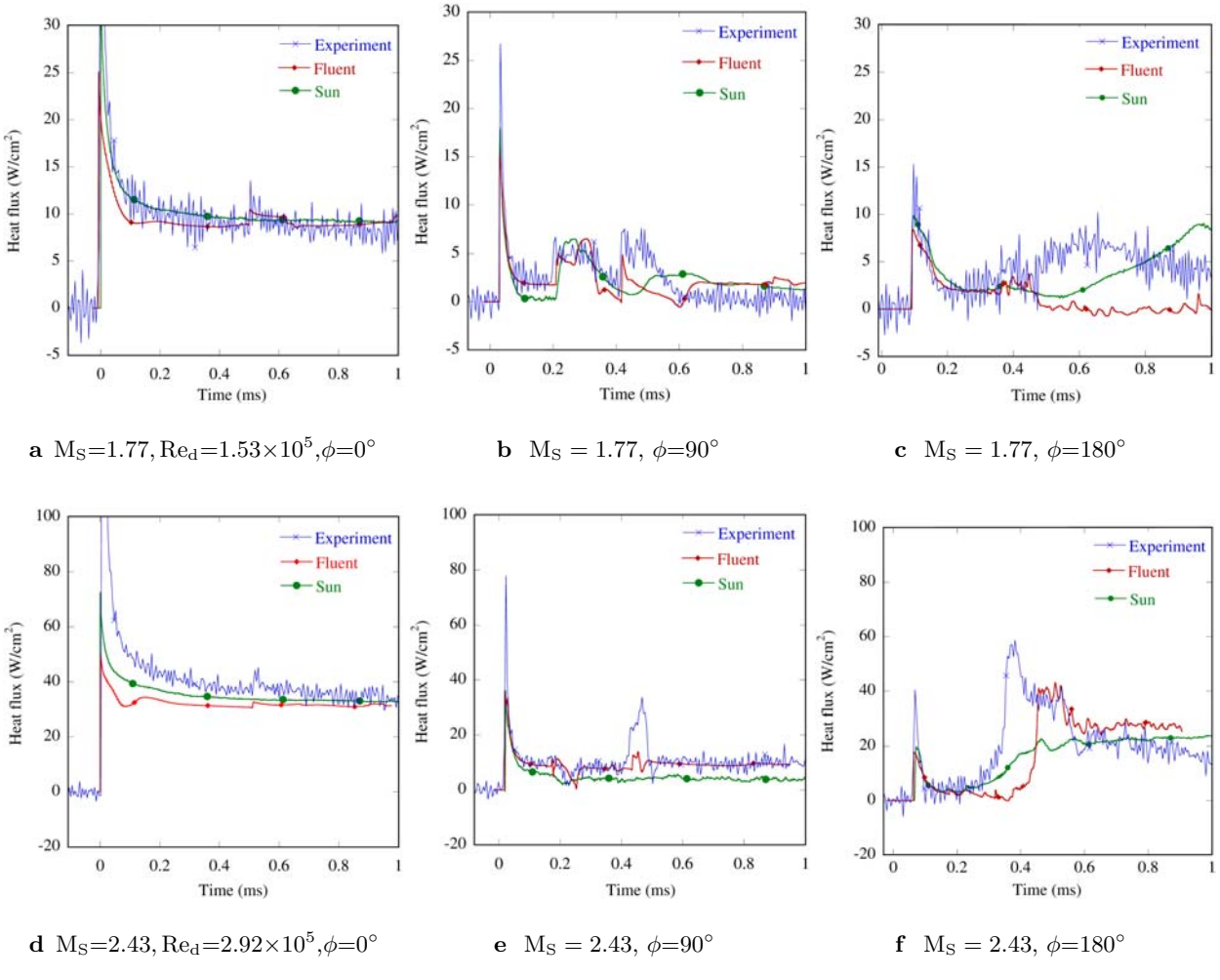


**a** $M_S$=1.77, $Re_d$=1.53×10$^5$,$\phi$=0° **b** $M_S$ = 1.77, $\phi$=90° **c** $M_S$ = 1.77, $\phi$=180°

**d** $M_S$=2.43, $Re_d$=2.92×10$^5$,$\phi$=0° **e** $M_S$ = 2.43, $\phi$=90° **f** $M_S$ = 2.43, $\phi$=180°

**Fig. 13a–f.** Comparison of experimental and numerical heat flux signals

Strouhal number has been calculated which works out to be $Sr = 0.151$ for the Reynolds number $5\times10^4$. For the rest of the Reynolds numbers in this study, the temperature readings do not show a regular frequency, which indicates that the vortex shedding may not be regular for these cases, though the temperature signals are unsteady with some momentary fluctuations.

### 3.2 Numerical simulations

The flow fields around the cylinder have been simulated using a laminar, two-dimensional unsteady Navier-Stokes solver, using the finite volume method on a solution-adaptive unstructured quadrilateral grid, which has been developed in house (Sun and Takayama, 1999). The two-step Runge-Kutta method is used to achieve second-order accuracy in time, and the second-order spatial accuracy is obtained by following the MUSCL-type data reconstruction. Given the data states on both sides of an interface, the inviscid flux through it is solved by an artificial upstream splitting method (Sun and Takayama, 2003). Viscous and heat conduction terms are made discrete by the central difference method. Numerical simulations have also been carried out using a commercial CFD code- *Fluent* (Version 6.1, Fluent Inc.) – a complete N-S solver, using a second-order explicit upwind scheme. The grid size in the boundary layer is 16 μm high, and the aspect ratio of the grid is about 2. The test gas is considered as a perfect gas with a constant ratio of specific heats, $\gamma = 1.4$. The isothermal boundary condition is assumed on the model surface, and its temperature is taken as that in front of the incident shock wave. No-slip conditions are specified for both the velocity components at the wall surface. The coefficients of viscosity and heat conductivity are varied with temperature following Sutherland's law.

Figure 12 gives the simulated temperature fields around the cylinder, obtained using the *Fluent* code. These pictures also indicate that the flow separation occurs after $\phi = 90°$, with a drop and unsteadiness in the temperature of the flow in the wake of the cylinder. No significant vortex shedding is noticed in the wake in the

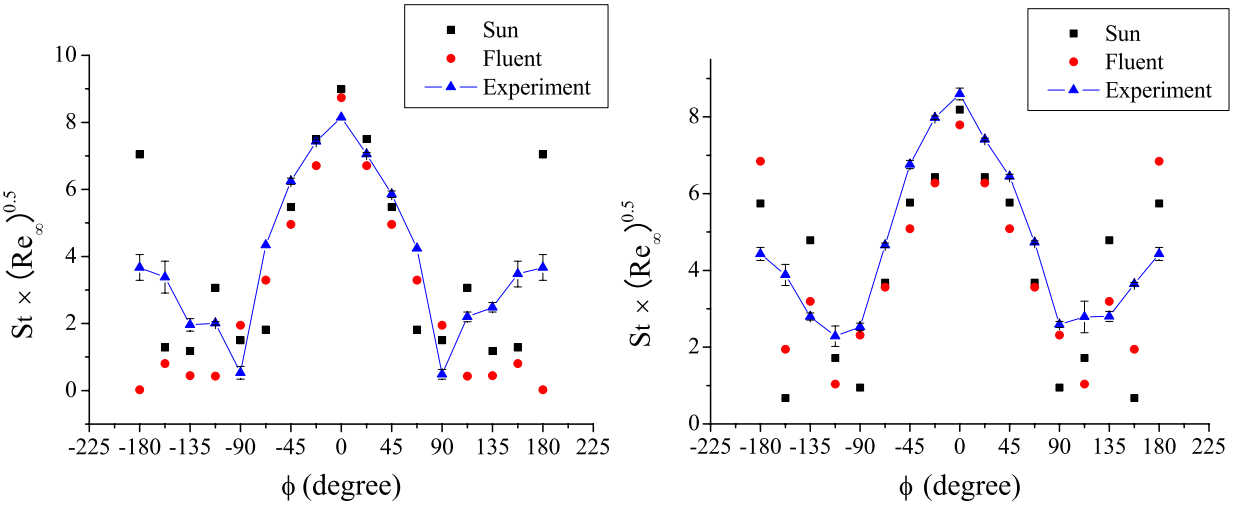


**a** $M_S = 1.77$, $Re_d = 1.53 \times 10^5$ **b** $M_S = 2.43$, $Re_d = 2.92 \times 10^5$

**Fig. 14a,b.** Comparison of experimental and numerical heat flux on a cylindrical surface

simulated flow fields except for $M_S$ 4.04, where a light vortex shedding is observed in the wake at the location between $\phi = 90°$ and 135°, which gives an insight into the periodic variations observed in the experimental temperature signals.

In the simulations carried out using the commercial code *Fluent*, the upper and lower boundaries of the test section of the shock tube were included in the computational domain and hence the cylinder bow shock is seen being reflected from the walls in the flow field pictures in Figs. 12c–f. The reflected shock from the wall is seen impinging on to the cylinder surface at around $\phi = 90°$ in Fig. 12f, which substantiates the second sudden rise in the temperature readings, after the jump caused by the incident shock wave, indicated in Fig. 11b, ($\phi$=90°). The simulated heat flux with respect to time at different locations on the cylinder surface are compared with the experimental heat flux signals in Fig. 13 for incident shock Mach numbers of 1.77 and 2.43.

The signals agree well with each other at one millisecond of time after the arrival of the incident shock on the model, with a small deviation in the unsteady flow region in the wake, where the flow could be turbulent.

A comparison between experimental and numerical heating rate distributions on the cylinder surface is presented in Fig. 14. The heat flux values presented in this figure have been averaged over 200 μs, from 0.8 to 1 ms on the time scale, after the arrival of incident shock wave at the model surface. Except at the early stage of shock/cylinder interaction, a significant difference between numerical solutions and experiments is seen. The flow over the front of the cylindrical model is rather simple; it is primarily an attached boundary layer with inviscid flow outside. Consequently, grid-converged numerical solutions are found in this region. In Sun's in-house code, the numerical cell size is controlled by varying the mesh refinement levels with increasing space resolution, e.g. Level 1, Level 2, and so on. It is found that the solutions are the same when the level is higher than, say, Level 3 depending on the initial background mesh sizes. The flow in this region is rather regular and the heat transfer rates agree reasonably well with experiments as shown in Figs. 13 and 14.

The numerical heat transfer rate on the rear side of the model where the flow is separated, depends strongly on the grid size employed and no grid convergence has been achieved in this region for any of the cases within the mesh refinement range. This can be expected since the resolution of the vortical structure in the wake is mainly determined by the numerical cell size. Also, in Sun's numerical simulations, the effect of the upper and lower wall of the shock tube is not included, hence the noticeable rise in heat flux at around 0.5 ms, as seen in Fig. 13 due to the shock reflection from the walls, which is absent in the results.

## 4 Conclusion

Heat flux to a cylinder has been measured in a shock tube and the measured values have been compared with the computed results from two CFD codes to complement the numerical as well as the experimental techniques. The flow physics predicted by the numerical results around the cylinder is in good agreement with the experimental signals, but the computed heat flux values at the surface of the cylinder exhibit a difference when compared to the measured values. This difference is moderate as far as the heat flux at the front end of the cylinder is concerned, but in the wake of the cylinder, the measured and computed values of heat flux deviate from each other by a larger magnitude. Though the values of convection dominated, quantities such as pressure, density etc., predicted

by these CFD codes are in very good agreement with the measured values. The results on viscous dominated quantities that are boundary layer sensitive, such as heat flux and skin friction, deviate from the measured ones. Further efforts are needed to resolve these differences, which means reliable, innovative, and carefully designed experimental techniques and facilities need to be progressed to complement the CFD studies.

*Acknowledgements.* The support rendered by Mr. T. Otomo, Mr. S. Hayasaka, Mr. T. Akama, Dr. W. Zhao, Mr. H. Ojima, and Mr. T. Ogawa during the course of this work is thankfully acknowledged. The authors would like to express their sincere thanks to Dr. H. Yamakawa of ULVAC Inc. for his help during the fabrication of the platinum thin film gauges. The financial assistance offered by the Grant-in-aid for Center of Excellence is gratefully acknowledged.

## References

Bearman, P.W.: On vortex shedding from a circular cylinder in the critical Reynolds number regime. J. Fluid Mech. **37**, 577–585 (1969)

Chang, P.K.: *Separation of flow.* Pergamon Press, Oxford (1970)

Cook, W.J., Felderman, E.J.: Reduction of data from thin film heat transfer gauges: A concise numerical technique. AIAA J. **4**, 561–562 (1966)

Hermann, D., Wesslau, F.P., Adomeit, G.: Measurements of heat transfer and vortex shedding frequency of cylinders in shock tube cross flow. In: Grönig, H., *Proc 16th ISSW*, Aachen, pp. 821–830 (1987)

Hollis, B.R.: User's manual for the one-dimensional hypersonic aero-thermodynamic (1DHEAT) data reduction code. NASA Contractor Rep. 4691 (1995)

Meguro, T., Takayama, K., Onodera, O.: Three-dimensional shock wave reflection over a corner of two intersecting wedges. Shock Waves **7**, 107–121 (1997)

Roshko, A.: Experiments on the flow past a circular cylinder at very high Reynolds number. J. Fluid Mech. **10**, 345–356 (1961)

Sun, M., Takayama, K.: Conservative smoothing on an adaptive quadrilateral grid. J. Computat. Phys. **150**, 143–180 (1999)

Sun, M., Takayama, K.: An artificial upstream flux vector splitting scheme for the Euler equations. J. Computat. Phys. **189**, 305–329 (2003)

Vidal, R.J.: Model instrumentation techniques for heat transfer and force measurements in a hypersonic shock tunnel. Cornell Aeronautical Lab. Rep. WADC TN 56–315 (1956)